Effect of confinement and octahedral rotations on the electronic, magnetic, and thermoelectric properties of correlated $SrXO_3/SrTiO_3(001)$ superlattices (X = V, Cr, or Mn)

Manish Verma,* Benjamin Geisler,† and Rossitza Pentcheva‡
Department of Physics and Center for Nanointegration (CENIDE), University of Duisburg-Essen, Lotharstrasse 1, 47057 Duisburg, Germany

(Received 24 May 2019; revised manuscript received 19 August 2019; published 16 October 2019)

By using density functional theory calculations with an on-site Coulomb repulsion term combined with Boltzmann transport theory, we explore the effect of t_{2g} orbital occupation on the electronic, magnetic, and thermoelectric properties of $(SrXO_3)_1/(SrTiO_3)_n(001)$ superlattices with $n = 1, 3$ and X = V, Cr, and Mn. In order to disentangle the effect of quantum confinement and octahedral rotations and to account for a wider temperature range, $P4/mmm$ (untilted) and $P2_1/c$ (tilted) phases are considered. We find that the ground-state superlattice geometries always display finite octahedral rotations, which drive an orbital reconstruction and a concomitant metal-to-insulator transition in confined $SrVO_3$ and $SrCrO_3$ single layers with ferro- and antiferromagnetic spin alignments, respectively. On the other hand, the confined $SrMnO_3$ single layer exhibits electronic properties similar to bulk. We show that confinement enhances the thermoelectric properties, particularly for $SrVO_3$ and $SrCrO_3$ due to the emergent Mott phase. Large room-temperature Seebeck coefficients are obtained for the tilted superlattices, ranging from 500 to 600 μV/K near the band edges. The estimated attainable power factors of 27.9 (26.6) $\mu W\,K^{-2}\,cm^{-1}$ in plane for the $(SrCrO_3)_1/(SrTiO_3)_1(001)$ superlattice with $P4/mmm$ ($P2_1/c$) symmetry and 28.1 $\mu W\,K^{-2}\,cm^{-1}$ cross plane for the $(SrMnO_3)_1/(SrTiO_3)_1(001)$ superlattice with $P2_1/c$ symmetry compare favorably with some of the best-performing oxide thermoelectrics. This demonstrates that the idea to use quantum confinement to enhance the thermoelectric response in correlated transition-metal oxide superlattices [Phys. Rev. Mater. **2**, 055403 (2018)] can be applied to a broader class of materials combinations.

DOI: 10.1103/PhysRevB.100.165126

I. INTRODUCTION

Thermoelectric materials directly convert heat into electricity and have important applications in energy recuperation and refrigeration. Transition-metal oxides constitute an important class of thermoelectric materials owing to their chemical and thermal stabilities as well as their environmental friendliness. Moreover, the strong correlations present in these materials play an important role in thermoelectrics [1,2] as they can considerably modify the band structure and induce peaks in the density of states, thereby increasing the Seebeck coefficient S according to Mott's formula [3,4]. Significant experimental and computational [5] research focuses on finding improved oxide thermoelectrics among bulk materials [6,7] by doping [8–10] or strain [11].

The performance of thermoelectric materials is determined by the figure of merit $ZT = \sigma S^2 T/\kappa$, where σ and κ denote the electrical and thermal conductivities, respectively. Hicks, Harman, and Dresselhaus [12] proposed that ZT can be improved in reduced dimensions, a route that has become viable owing to modern layer-by-layer growth techniques that enable an atomic-scale design of artificial transition-metal oxide heterostructures [13–17]. The role of quantum confinement and interface polarity to enhance and design thermoelectricity have been assessed for the prominent $LaAlO_3/SrTiO_3$ (LAO/STO) system [18–20] as well as for $(LaNiO_3)/(SrTiO_3)(001)$ (LNO/STO) [21] and $(LaNiO_3)/(LaAlO_3)(001)$ superlattices (SLs) [22,23].

Recent work has demonstrated that the thermoelectric response in $(LaNiO_3)_1/(LaAlO_3)_1(001)$ SLs is significantly enhanced [22]. This is attributed to the metal-to-insulator transition accompanied by bond and charge disproportionations [24], induced by the interplay of quantum confinement and tensile epitaxial strain. This concept directly exploits the correlation effects in transition-metal oxides and, thus, extends beyond the proposal of Hicks, Harman, and Dresselhaus [12]. The question arises whether this strategy can be successfully applied also to other materials combinations.

Systems based on the band insulator $SrTiO_3$ are known for their excellent thermoelectric properties [25–27] and, therefore, emerge as ideal test cases. Okuda *et al.* reported a power factor of σS^2 of 28–36 $\mu W\,K^{-2}\,cm^{-1}$ at 300 K for heavily La-doped single crystals [28]. Ohta *et al.* achieved a power factor of $\sim$20 $\mu W\,K^{-2}\,cm^{-1}$ at 300 K in Nb-doped single crystals [29]. In these systems, doping leads to partial occupation of the Ti $3d$ orbitals, which are, thus, the physically active states.

In this paper, we focus instead on the nonpolar $(SrXO_3)_1/(SrTiO_3)_n(001)$ SLs with $n = 1, 3$ and X = V (d^1), Cr (d^2), and Mn (d^3). While in these systems the Ti $3d$ orbitals are formally empty (d^0) and play no active role, we systematically explore the effect of confinement and t_{2g} orbital occupation of the X^{4+} ion on the electronic, magnetic, and thermoelectric properties. A further advantage of SLs over bulk systems is the possible reduction of the lattice thermal conductivity. Indeed, a large interface thermal

*manish.verma@uni-due.de
†benjamin.geisler@uni-due.de
‡rossitza.pentcheva@uni-due.de

resistance was found recently in $(SrVO_3)/(SrTiO_3)(001)$ [(SVO)/(STO)(001)] SLs by Katsufuji *et al.* despite the similar phononic properties of the constituent bulk compounds [30]. We consider both tetragonal ($P4/mmm$, untilted) and monoclinic ($P2_1/c$, tilted) structures. Our density functional theory (DFT) calculations including an on-site Coulomb repulsion term find that the studied SLs exhibit finite octahedral rotations and tilts. For $SrVO_3$ and $SrCrO_3$ (SCO) single layers confined in $SrTiO_3$, already small octahedral rotations trigger a significant electronic reconstruction towards orbital order together with ferromagnetic (FM) and antiferromagnetic (AFM) spin alignments, respectively. This is accompanied by a metal-to-insulator transition. On the other hand, a confined $SrMnO_3$ (SMO) single layer shows electronic properties similar to bulk and only modest octahedral rotations.

Moreover, we provide in- and cross-plane electronic transport and thermoelectric quantities by using Boltzmann transport theory in the constant relaxation time approximation. We find large room-temperature Seebeck coefficients ranging from 500 to 600 μV/K in the vicinity of the band edges for the tilted $(SrVO_3)_1/(SrTiO_3)_1(001)$ and $(SrCrO_3)_1/(SrTiO_3)_1(001)$ SLs due to the metal-to-insulator transition, whereas $(SrMnO_3)_1/(SrTiO_3)_1(001)$ SLs show a very good thermoelectric performance irrespective of octahedral rotations. The estimated attainable power factors exceed those of $(LaNiO_3)_1/(LaAlO_3)_1(001)$ SLs [22] by more than a factor of 2 and compare favorably with some of the best-performing oxide thermoelectrics, such as La- or Nb-doped $SrTiO_3$ [27–29]. This demonstrates that the confinement-induced metal-to-insulator transition can substantially enhance the thermoelectric performance in correlated artificial transition-metal oxides.

II. METHODS

First-principles calculations for $(SrXO_3)_1/(SrTiO_3)_n(001)$ SLs with $X = V$, Cr, and Mn and $n = 1, 3$ (referred to as 1/1 SL and 1/3 SL, respectively) have been performed in the framework of spin-polarized DFT [31] by using the linearized augmented plane-wave method as implemented in the all-electron full-potential code WIEN2K [32]. We used $R_{MT} \times K_{max} = 7$ along with R_{MT} values of 2.46 a.u. for Sr, 1.83 a.u. for Ti, V, Cr, and Mn, and 1.65 a.u. for O. The PBEsol exchange-correlation functional [33] has been employed as it renders a better description of the structural properties. In order to take static correlation effects into account, the DFT + U approach [34] with $U = 5$ and $J = 0.7$ eV for V, Cr, Mn, and Ti $3d$ states was used. For selected cases, the dependence on U has been studied in more detail. These values are in line with previous studies [21,35–37]. To sample the Brillouin zone, we have used $8 \times 8 \times 4$ and $8 \times 8 \times 2$ Monkhorst-Pack k-point grids [38] for the 1/1 and 1/3 SLs, respectively. In order to take octahedral tilts fully into account, we model the 1/1 (1/3) SLs by using $\sqrt{2}a \times \sqrt{2}a \times 2c$ ($4c$) supercells rotated by 45° about the [001] axis with respect to the cubic perovskite unit cell that contain 20 (40) atoms in total. The in-plane lattice constant was fixed to the experimental lattice constant of STO, $a = 3.905$ Å, modeling epitaxial growth on a STO(001) substrate, whereas the c parameter along with the internal positions were optimized. The BOLTZTRAP code [39] was employed to provide the energy- and spin-resolved transmission $T_\sigma(E)$ from the DFT electronic structure by using Boltzmann transport theory in the constant relaxation time approximation. We obtained converged transmission curves for $38 \times 38 \times 26$ and $38 \times 38 \times 13$ k points for the 1/1 and 1/3 SLs, respectively. Subsequently, we have calculated the thermoelectric quantities by using the approach of Sivan and Imry [40], which has been described and used in previous studies [10,11,21–23,41–43].

III. BULK $SrXO_3$, X = V, Cr, AND Mn

We start by providing a short overview of bulk properties for the three compounds that are to be confined later in the band insulator STO (d^0). Note that the latter adopts a cubic $Pm\bar{3}m$ structure around room temperature and undergoes a transition to an antiferrodistortive tilted phase only below 105 K [44].

The correlated metal SVO (d^1) crystallizes in a cubic perovskite structure (space group $Pm\bar{3}m$) with a lattice parameter of $a = 3.84$ Å [45–51]. Although actually paramagnetic, there is also experimental [52] and theoretical [35] evidence for a FM phase with $1\mu_B$ per V site.

SCO (d^2) is a cubic perovskite with $a = 3.818$ Å and a paramagnetic metal at room temperature [53]. For $T < 100$ K, a tetragonal C-type AFM phase with space group $P4/mmm$ exists [54,55]. Theoretical studies confirm C-type AFM order in the tetragonal phase along with $(d_{xy})^1(d_{xz}, d_{yz})^1$ orbital order [36,56]. Consistently, SCO(001) thin films were found to be AFM ordered and metallic below 100 K, possibly with orbital order [57].

Although the ground state of SMO (d^3) is hexagonal, a cubic $Pm\bar{3}m$ phase with lattice parameter $a = 3.805$ Å [58] can be stabilized at room temperature [59]. It is semiconducting

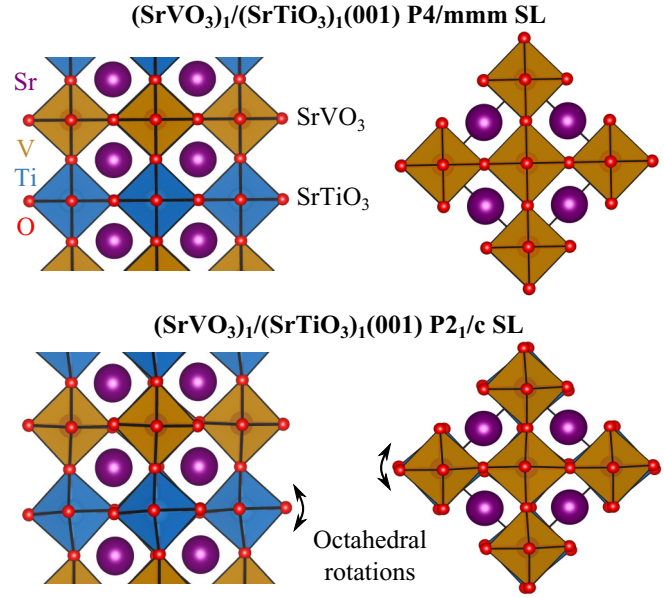

FIG. 1. Side and top view of optimized $(SrVO_3)_1/(SrTiO_3)_1(001)$ SLs with $P4/mmm$ symmetry (untilted, top row) and with $P2_1/c$ symmetry where octahedral tilts and rotations are fully considered (bottom row).

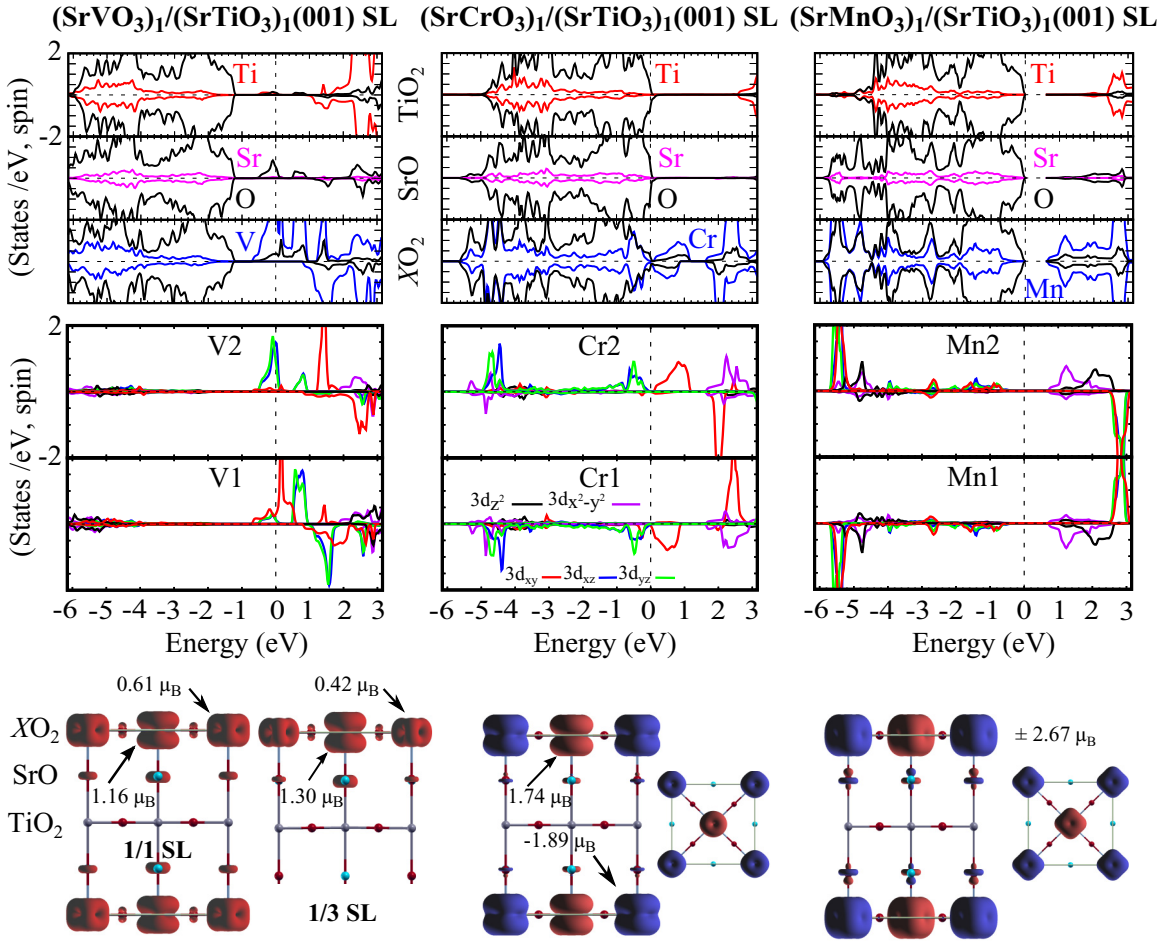

FIG. 2. Projected densities of states and corresponding spin densities of tetragonal $(SrXO_3)_1/(SrTiO_3)_1(001)$ SLs ($P4/mmm$ symmetry) with X = V, Cr, and Mn. Top row: Layer-, element-, and spin-resolved densities of states for the TiO_2, SrO, and XO_2 layers. Central row: Site-, orbital-, and spin-resolved densities of states for the two distinct X sites. Bottom row: Spin densities (side and top views), integrated from −6 eV to the Fermi energy (0 eV), together with the local magnetic moments at the two distinct X sites. The spin density of the vanadate 1/3 SL is shown for comparison. Red and blue correspond to positive/negative spin densities.

and adopts G-type AFM order with a Mn magnetic moment of $\sim 2.6\mu_B$ [60,61] and a Néel temperature between 233 and 260 K [60,62,63]. SMO has also been grown as a thin film on various substrates [64–66] and as a SL, e.g., with $LaMnO_3$ on STO(001) [67].

IV. $(SrXO_3)_1/(SrTiO_3)_n(001)$, X = V, Cr, AND Mn SUPERLATTICES WITH $P4/mmm$ SYMMETRY

We now discuss the structural, electronic, and magnetic properties of SLs in which single layers of SVO, SCO, and SMO are confined in $n = 1, 3$ layers of the band insulator STO as displayed exemplarily in Fig. 1 for the $(SVO)_1/(STO)_1(001)$ SL. In order to disentangle the effect of quantum confinement and octahedral rotations, we start with SLs of metastable $P4/mmm$ symmetry (i.e., without tilts), before moving later to their distorted ground states with $P2_1/c$ symmetry.

When constrained to the lateral lattice constant of the STO substrate ($a = 3.905$ Å) the optimized cross-plane lattice constants are $c = 3.87$, 3.88, and 3.83 Å in 1/1 SLs and $c = 3.91$, 3.87, and 3.83 Å in 1/3 SLs for X = V, Cr, and Mn, respectively. Detailed structural parameters for the SLs are provided in the Supplemental Material [68] together with an analysis of the impact of on-site Coulomb repulsion on the octahedral rotations.

A. $(SrVO_3)_1/(SrTiO_3)_n(001)$ superlattices

We begin with $(SVO)_1/(STO)_n(001)$ SLs (d^1/d^0). For the 1/3 SL, we find FM order to be more stable than AFM order. The partial occupation of the degenerate t_{2g} orbitals is accommodated by a checkerboard $V^{4+} \rightarrow V^{4+\delta} + V^{4-\delta}$ charge disproportionation (CD) at the V sites, which goes hand in hand with a breathing mode distortion of the VO_6 octahedra (octahedral volumes: 9.34/10.43 Å^3 at the V1/V2 sites, respectively). The basal/apical V-O bond lengths are 1.92/1.91 Å at the V1 site and 1.99/1.98 Å at the V2 site. The CD is also reflected in distinct spin magnetic moments of $0.42/1.30\mu_B$ at the two V sites as indicted in the spin-density plot shown in Fig. 2. Interestingly, we obtain a similar, albeit less pronounced CD breathing-mode phase for the 1/1 SL as well. Again, FM order is more stable than AFM order with V1/V2 magnetic moments of $0.61/1.16\mu_B$ corresponding

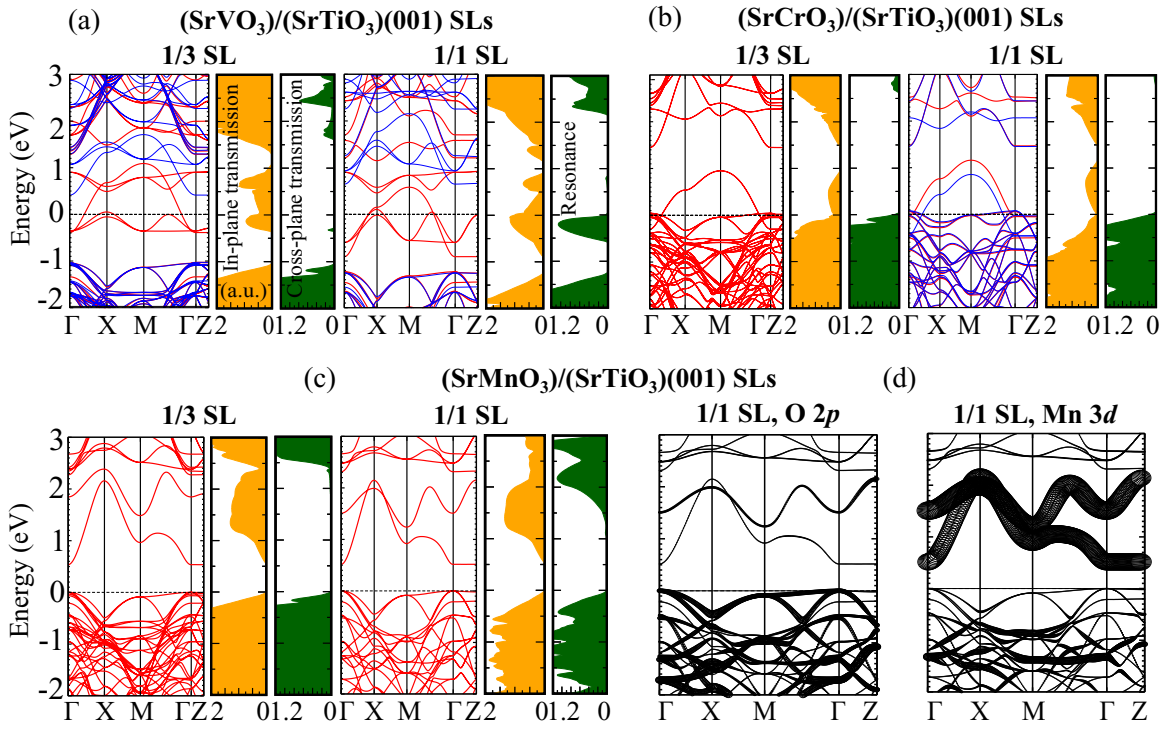

FIG. 3. Band structure and in- and cross-plane majority-spin transmission $\mathcal{T}_{\uparrow}(E)$ of tetragonal $(SrXO_3)_1/(SrTiO_3)_n(001)$ SLs ($P4/mmm$ symmetry) with $n = 1, 3$ and (a) $X =$ V, (b) Cr, and (c) Mn. Red and blue bands correspond to spin-up and spin-down channels, respectively. For the $(SrMnO_3)_1/(SrTiO_3)_1(001)$ SL, additional band character plots (d) show the contributions of O $2p$ and Mn $3d$ orbitals in the confined MnO_2 single layer.

to alternating smaller (9.44 $Å^3$) and bigger (10.10 $Å^3$) VO_6 octahedra. Despite this electronic reconstruction, both 1/3 and 1/1 SLs are metallic due to V $3d_{xy}$ states crossing the Fermi energy.

We observe the CD phase only for $U > 3.5$ eV ($J = 0.7$ eV), irrespective of n. For $U < 3.5$ eV, a metallic phase is obtained as well, but the electron distribution is uniform among the V sites. With increasing on-site Coulomb repulsion, CD is enhanced: At $U = 6$ eV, we find magnetic moments of $1.46/0.2\mu_B$ and an emerging band gap of 0.27 eV, whereas at $U = 7$ eV magnetic moments of $1.53/0.12\mu_B$ and a band gap of 0.64 eV are obtained.

The tendency to counter orbital degeneracy by CD is a well-known phenomenon in bulk $YNiO_3$ and $LuNiO_3$ [69] and layered nickelates, such as $(LaNiO_3)_1/(LaAlO_3)_1(001)$ SLs [22,24] or cuprate-nickelate hybrid structures [70]. Notably, our finding of a breathing-mode CD phase in 1/3 and 1/1 SLs is distinct from the results obtained by Pardo and Pickett in related untilted $(SVO)_1/(STO)_4(001)$ SLs, i.e., a FM metallic orbital-ordered state with uniform and strong V $3d_{xy}$ occupation that turns insulating under the presence of spin-orbit coupling [35]. We will show below that octahedral rotations are an alternative and strong driving force to open a band gap.

From the TiO_2 panels of the projected density of states (Fig. 2), we infer that the Fermi energy is located in the center of the STO band gap, pinned by V $3d$ states. Analysis of the band structure (Fig. 3) shows that a reduction of the confining STO thickness from $n = 3$ to $n = 1$ lowers the energy of the V $3d_{xy}$ bands by ∼0.5 eV and increases the bandwidth of the V $3d_{xz}$ and $3d_{yz}$ bands from 0.4 to 0.7 eV. Moreover, it increases the Γ-Z dispersion of the V $3d$ states, which results in the formation of a sizable resonance in the cross-plane transmission right below the Fermi energy. This resonance stems from V $3d_{xz}$ and $3d_{yz}$ states that hybridize strongly with $2p$ states of apical oxygen atoms (Fig. 2); it significantly enhances the cross-plane thermoelectric response as we will discuss below. We see that even without octahedral tilts as additional degrees of freedom, quantum confinement strongly impacts the electronic structure of vanadate SLs, and not exclusively in the vertical direction (i.e., along Γ-Z).

B. $(SrCrO_3)_1/(SrTiO_3)_n(001)$ superlattices

In $(SCO)_1/(STO)_n(001)$ SLs (d^2/d^0), we observe a metallic AFM state in both 1/1 and 1/3 SLs (Figs. 2 and 3). Increasing U destabilizes AFM order, and beyond $U = 6$ eV FM order becomes the ground state. Such competing FM/AFM order is typical for Cr compounds [71]: The $(SCO)_1/(STO)_n$ SLs are isoelectronic to half-metallic FM CrO_2 in which strain or doping can induce a transition to AFM order [72,73] as well as to insulating AFM YVO_3 or $LaVO_3$ [74,75].

The projected density of states (Fig. 2) shows that the Cr $3d_{xz}$ and $3d_{yz}$ orbitals are occupied at each Cr site, whereas the $3d_{xy}$ orbital is empty and higher in energy related to the small vertical compression of the CrO_6 octahedra (basal/apical V-O bond lengths: 1.95/1.93 Å for the 1/1 SL). In contrast to the 1/3 SL (Fig. 3) and the 1/1 SL with octahedral tilts (discussed below), we observe a slight difference in orbital occupation at the two Cr sites present in the 1/1 SL, reflected

in spin magnetic moments of -1.89 and $1.74\mu_B$ (Fig. 2) and noncongruent band structures in the two spin channels (Fig. 3).

The Fermi energy is aligned with the valence-band maximum (VBM) of the STO region. By reduction of the confining STO region, the Cr-3d bands become more dispersive along the Γ-Z direction (Fig. 3), thereby increasing the cross-plane conductivity. However, the overall impact of varying the confinement is less pronounced here than for the V-based SLs discussed above.

C. $(SrMnO_3)_1/(SrTiO_3)_n(001)$ superlattices

In $(SMO)_1/(STO)_n(001)$ SLs (d^3/d^0), the t_{2g} orbitals are half-filled. This leads to band gaps of 0.54 and 0.53 eV in 1/3 and 1/1 SLs, respectively, which are close to the value we find for bulk SMO (0.5 eV). The VBM of the MnO_2 layer is aligned with the VBM of the STO region (cf. Fig. 2). As a result of the tensile strain, the MnO_6 octahedra are compressed with basal and apical Mn-O bond lengths of 1.95 and 1.87 Å, respectively, in both 1/3 and 1/1 SLs. AFM order was found to be more stable than FM order in both 1/3 and 1/1 SLs along with Mn magnetic moments of $\pm 2.67\mu_B$ as shown in the spin-density plot in Fig. 2, similar to bulk SMO. The projected density of states (Fig. 2) and band character plots (Fig. 3) show that the VBM is formed by O 2p states in all layers. The Mn t_{2g} states are dispersed -0.5 eV below the VBM, whereas the e_g states constitute the conduction band. We therefore conclude that the band gap in the present SLs is of charge-transfer type, similar to bulk $SrMnO_3$ and $CaMnO_3$ [61,76,77].

Reduction of the STO thickness causes the Mn-3d bands to become more dispersive along the Γ-Z direction, which is particularly evident for the unoccupied Mn 3d e_g states (Fig. 3). Apart from these observations, the impact of varying the confinement is less pronounced here than for the V-based SLs discussed above.

V. $(SrXO_3)_1/(SrTiO_3)_n(001)$, X = V, Cr, AND Mn SUPERLATTICES WITH $P2_1/c$ SYMMETRY

We now allow octahedral rotations to emerge as additional degrees of freedom, which lowers the symmetry to $P2_1/c$. Irrespective of X and n, we found structures with finite antiferrodistortive octahedral rotations to be the ground state (Table I). Exemplarily, Fig. 1 shows the optimized geometry of the $(SVO)_1/(STO)_1(001)$ SL. Even though the rotational angles are small, as detailed below, the impact on the electronic structure of the SLs is very strong.

TABLE I. Stabilization [total energy difference $\Delta E = E(P4/mmm) - E(P2_1/c)$ per TM atom] of different SLs due to octahedral rotations.

System	ΔE (meV), $n = 1$	ΔE (meV), $n = 3$
$(SVO)_1/(STO)_n$ SL	298	326
$(SCO)_1/(STO)_n$ SL	224	243
$(SMO)_1/(STO)_n$ SL	7	46

The optimized cross-plane lattice constants are 3.90, 3.84, and 3.83 Å in 1/1 SLs and $c = 3.89$, 3.83, and 3.83 Å in 1/3 SLs for X = V, Cr, and Mn, respectively. Further details about the structural parameters are provided in the Supplemental Material [68].

A. $(SrVO_3)_1/(SrTiO_3)_n(001)$ superlattices

We find that octahedral rotations stabilize the $(SVO)_1/(STO)_n$ 1/1 and 1/3 SLs by 298 and 326 meV per V atom, respectively, as compared to $P4/mmm$ symmetry (Table I). FM order is more stable than AFM order by 8 and 18 meV per V atom in the 1/1 and 1/3 SLs, respectively, with V magnetic moments of $0.85\mu_B$. Despite the small rotational angles (basal V-O-V bond angle $\sim 175^\circ$ and apical V-O-Ti bond angle $\sim 173^\circ$; 180° equals untilted), a Mott-insulating phase emerges with band gaps of 0.68 and 0.8 eV in the 1/1 and 1/3 SLs, respectively. Perfect orbital order is observed instead of CD, reflected in the spin-density plots (Fig. 4) with alternating 3d_{xz} and 3d_{yz} orbital occupation at the two V sites (checkerboard). At variance with the $P4/mmm$ SLs, the V 3d_{xy} band is always empty (Figs. 4 and 5). Right above the VBM of STO, a hybrid state is formed by V 3d and apical O 2p orbitals that even shows considerable contributions from the confining TiO_2 layer (Fig. 4).

Considering the strong energy gain associated with the octahedral rotations (Table I), this constitutes the ground state compared to the previously addressed CD phase in the $P4/mmm$ V-based SL and the tetragonal $(SVO)_1/(STO)_4(001)$ SL by Pardo and Pickett [35]. The associated orbital ordering opens a band gap in confined SVO single layers even without spin-orbit coupling. Additional calculations combining octahedral rotations *and* spin-orbit coupling lead to the same electronic phase, albeit exhibiting a larger band gap (2.1 eV) and a total energy additionally lowered by 97 meV per V atom (see the Supplemental Material [68]).

As we reduce the STO thickness from $n = 3$ to $n = 1$, the bands corresponding to the mentioned hybrid state at the VBM become more dispersive, in particular, along the Γ-Z direction (Fig. 5). This results in a cross-plane transmission peak together with a small increase in the in-plane transmission, whereas, in the 1/3 SL, there is almost no cross-plane transmission due to the larger STO tunneling barrier. The cross-plane transmission peak in the 1/1 SL is less pronounced in the tilted (Fig. 5) than in the untilted (Fig. 3) case owing to the distinct orbital occupation.

B. $(SrCrO_3)_1/(SrTiO_3)_n(001)$ superlattices

Octahedral rotations stabilize the $(SCO)_1/(STO)_n$ 1/1 and 1/3 SLs by 224 and 243 meV per Cr atom, respectively, as compared to $P4/mmm$ symmetry (Table I). Checkerboard AFM order is now clearly preferred over FM order by 23 and 27 meV per Cr atom in the 1/1 and 1/3 SLs, respectively, with Cr magnetic moments of $\pm 1.76\mu_B$. We find this magnetic order to be superimposed by alternating $d_{xy} + d_{xz}$, $d_{xy} + d_{yz}$ orbital order, similar to low-temperature bulk SCO [36,56], thereby opening band gaps of 0.97 and 1.15 eV in the 1/1 and 1/3 SLs, respectively (Figs. 4 and 5). Magnetic and

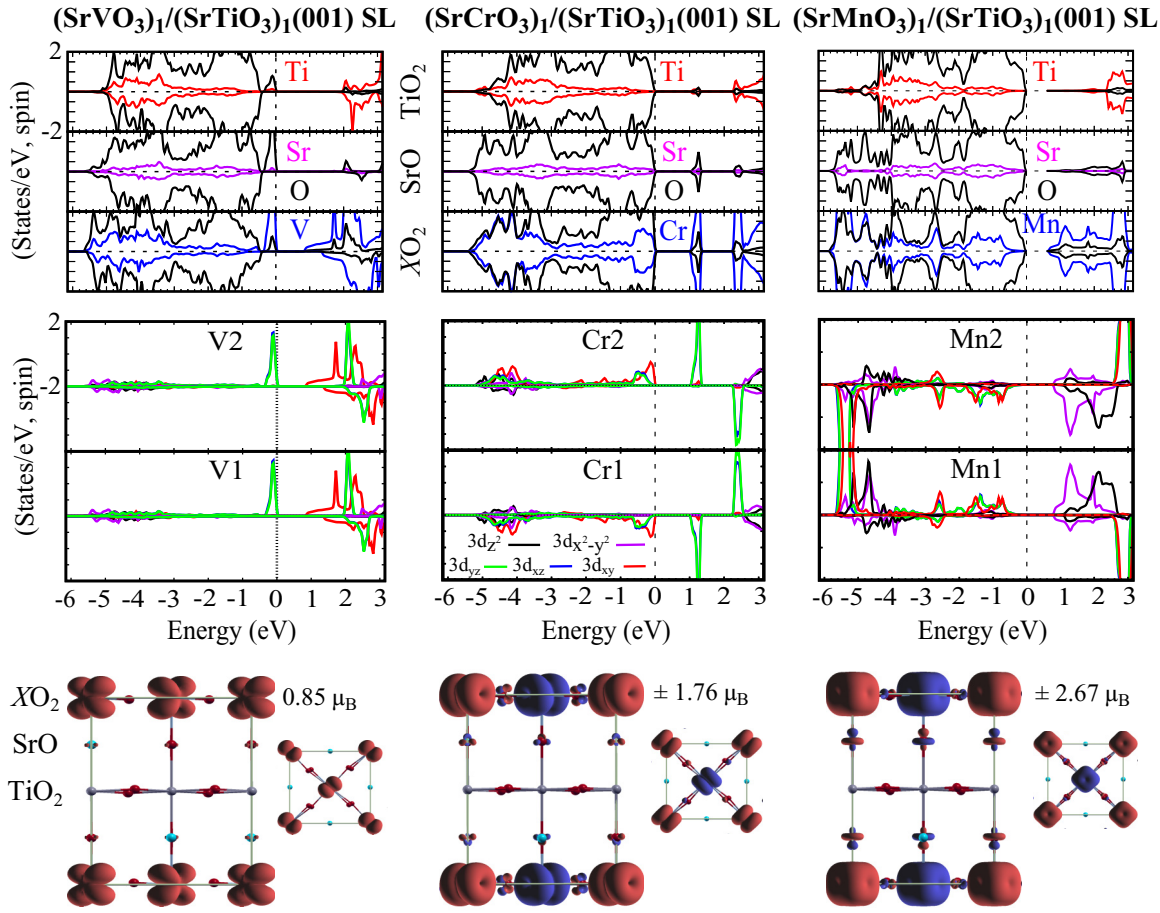

FIG. 4. Projected densities of states and corresponding spin densities of tilted $(SrXO_3)_1/(SrTiO_3)_1(001)$ SLs ($P2_1/c$ symmetry) with X = V, Cr, and Mn. Top row: Layer-, element-, and spin-resolved densities of states for the TiO_2, SrO, and XO_2 layers. Central row: Site-, orbital-, and spin-resolved densities of states for the two distinct X sites. Bottom row: Spin densities (side and top views), integrated from -6 eV to the Fermi energy (0 eV) together with the local magnetic moments at the two distinct X sites. In contrast to the untilted SLs, clear orbital order without charge or bond disproportionation emerges for the tilted V- and Cr-based SLs due to the extended degrees of freedom, accompanied by a metal-to-insulator transition.

orbital order can be directly inferred from the spin-density plots (Fig. 4). The orbital order is clearly distinct from that of the $P4/mmm$ SL discussed above, where d_{xz} and d_{yz} were occupied and the d_{xy} orbital was always empty at each site. Again, the octahedral rotations are small, for instance, the basal Cr-O-Cr bond angle and the apical Cr-O-Ti bond angle are $\sim 176^\circ$. It is interesting to note that the isoelectronic but more strongly tilted compound YVO_3 also shows $d_{xy} + d_{xz}$, $d_{xy} + d_{yz}$ orbital order (albeit of C-type) together with G-type AFM order [78–80].

The VBM of the CrO_2 layer is aligned with the VBM of the STO region (Fig. 4). Reducing the STO thickness from $n = 3$ to $n = 1$ increases the dispersion of the Cr $3d$ bands along the Γ-Z direction but leaves the overall band structure and transmission largely unchanged (Fig. 5).

C. $(SrMnO_3)_1/(SrTiO_3)_n(001)$ superlattices

In the case of $(SMO)_1/(STO)_n$ SLs, the energy difference between the $P4/mmm$ and the $P2_1/c$ symmetry is 7 and 46 meV per Mn atom in the 1/1 and 1/3 SLs, respectively, which is much smaller than in the V- and Cr-based SLs (Table I). These small energy differences correlate with the small octahedral rotation angles (basal Mn-O-Mn bond angle and apical Mn-O-Ti bond angle $\sim 174^\circ$). Consequently, we find the electronic structure and magnetic moments of the tilted SL (Fig. 5) to be similar to those of the untilted SL (Fig. 3), i.e., no electronic reconstruction is triggered by the octahedral rotations. The band gaps are slightly enlarged to 0.61 and 0.60 eV in the 1/1 and 1/3 SLs, respectively. Again, the VBM of the MnO_2 layer is aligned with the VBM of the STO region (Fig. 4).

VI. THERMOELECTRIC PERFORMANCE

We now discuss the thermoelectric properties of $(SXO)_1/(STO)_n(001)$ SLs, specifically their evolution with increasing t_{2g} orbital occupation (X = V, Cr, and Mn) and the impact of octahedral rotations. We focus on 1/1 SLs ($n = 1$) that tend to show an improved thermoelectric performance with respect to 1/3 SLs and in order to compare with the $(LNO)_1/(LAO)_1(001)$ SLs [22].

The thermoelectric properties are summarized in Fig. 6 and Table II. We report power factors divided by the relaxation

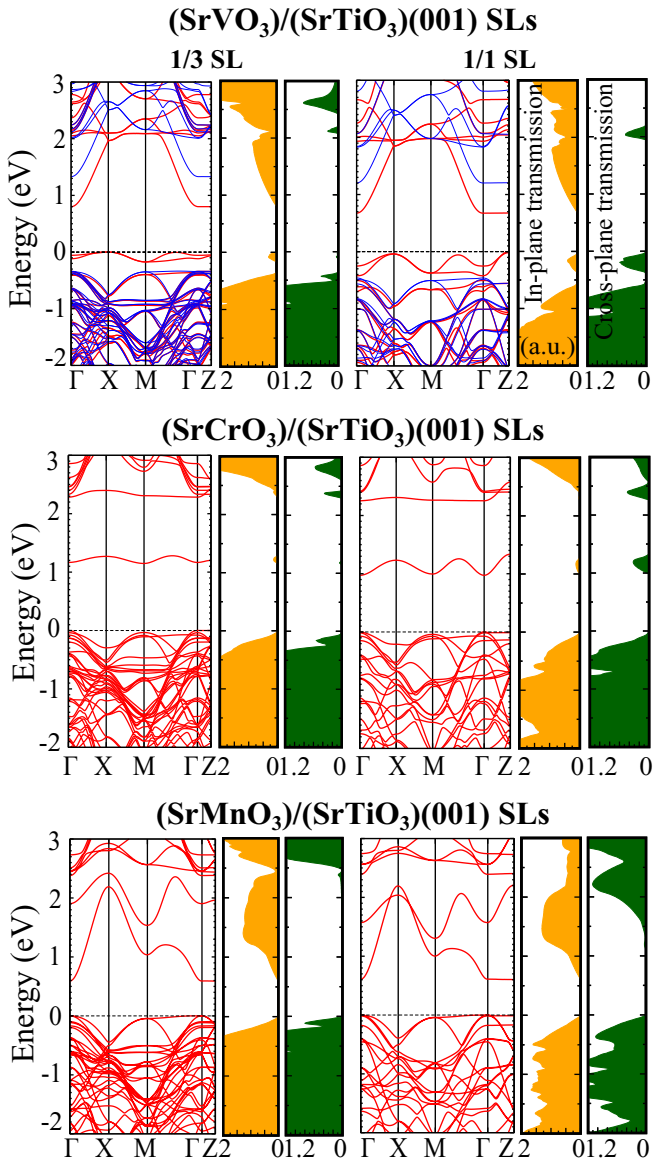

FIG. 5. Band structure and in- and cross-plane majority-spin transmission $\mathcal{T}_\uparrow(E)$ of tilted $(SrXO_3)_1/(SrTiO_3)_n(001)$ SLs ($P2_1/c$ symmetry) with $n = 1, 3$ and $X =$ V, Cr, and Mn. Red and blue bands correspond to spin-up and spin-down channels, respectively.

time PF/τ in Fig. 6 which are, hence, independent of the choice of τ and related to the electronic fitness function introduced by Xing *et al.* [81]. For Table II, we use a room-temperature relaxation time of $\tau = 4$ fs, a typical value for oxides and, particularly, for STO [19,22].

For values of the chemical potential μ that lie deep in the band gap, the Seebeck coefficient S can easily exceed 1000 μV/K (Fig. 6). However, the electrical conductivity σ and, thus, the PF decreases rapidly in the band gap. We therefore focus our discussion on μ values within a ±100-meV interval around the band edges. For the metallic systems, the Fermi energy cannot be controlled strongly by doping; therefore, we consider a smaller μ interval in that case. The values in the following refer to 300 K.

TABLE II. Overview of the attainable thermoelectric performance of the present $(SrXO_3)_1/(SrTiO_3)_1(001)$ SLs of different symmetries and comparison to a selection of prominent oxide thermoelectrics around room temperature (300 K). Further data concerning the 1/3 SLs can be found in the Supplemental Material [68].

System	S (μV/K)	PF (μW K^{-2} cm^{-1})
$P4/mmm$ symmetry, $\tau = 4$ fs		
$(SrVO_3)_1/(SrTiO_3)_1(001)$		
In plane	26	3.0
Cross plane	191	25.4
$(SrCrO_3)_1/(SrTiO_3)_1(001)$		
In plane	14	0.5
Cross plane	126	27.9
$(SrMnO_3)_1/(SrTiO_3)_1(001)$		
In plane	519	19.2
Cross plane	529	23.4
$P2_1/c$ symmetry, $\tau = 4$ fs		
$(SrVO_3)_1/(SrTiO_3)_1(001)$		
In plane	591	9.3
Cross plane	557	14.3
$(SrCrO_3)_1/(SrTiO_3)_1(001)$		
In plane	578	26.6
Cross plane	590	18.6
$(SrMnO_3)_1/(SrTiO_3)_1(001)$		
In plane	527	23.0
Cross plane	526	28.1
Literature		
$(LaNiO_3)_1/(LaAlO_3)_1(001)$, a_{STO}	(DFT + U [22], $\tau = 4$ fs)	
In plane	±600	11
Cross plane	±600	2
$SrTiO_3$ (DFT [19], $\tau = 4.3$ fs)	−400	10
La:$SrTiO_3$ bulk, expt. [28]	−380	35
La:$SrTiO_3$ films, expt. [27]	−980	39
Nb:$SrTiO_3$ bulk, expt. [29]	−240	20

We begin with a discussion of the $P4/mmm$ systems. Although the in-plane thermoelectric performance is small in the V- and Cr-based SLs, we find very large cross-plane PFs of 25.4 and 27.9 μW K^{-2} cm^{-1}, respectively, i.e., strongly anisotropic properties (Table II). This is related to the high Seebeck coefficients $S \sim 191$ and 126 μV/K in conjunction with high (metallic) electrical conductivities σ. For the Mn-based SLs, much higher $S \sim 519/529$ μV/K values are obtained in plane/cross plane owing to the presence of a small band gap. The PFs are also high (19.2/23.4 μW K^{-2} cm^{-1}), albeit smaller than in the cross-plane direction for the V- and Cr-based SLs.

The metal-to-insulator transition in the confined SVO and SCO single layers (Figs. 4 and 5) triggered by the small octahedral rotations in the $P2_1/c$ SLs has a drastic influence on the thermoelectric properties. Due to the band gap, the Seebeck coefficients get strongly enhanced and exceed even those we obtained for the Mn-based SL (Table II). This is accompanied by an increase of the in-plane PFs for the V-based SL and, particularly, for the Cr-based SL, reaching 9.3 and 26.6 μW K^{-2} cm^{-1}, respectively, at the expense of slightly lowered cross-plane PFs. For the Mn-based SL, we

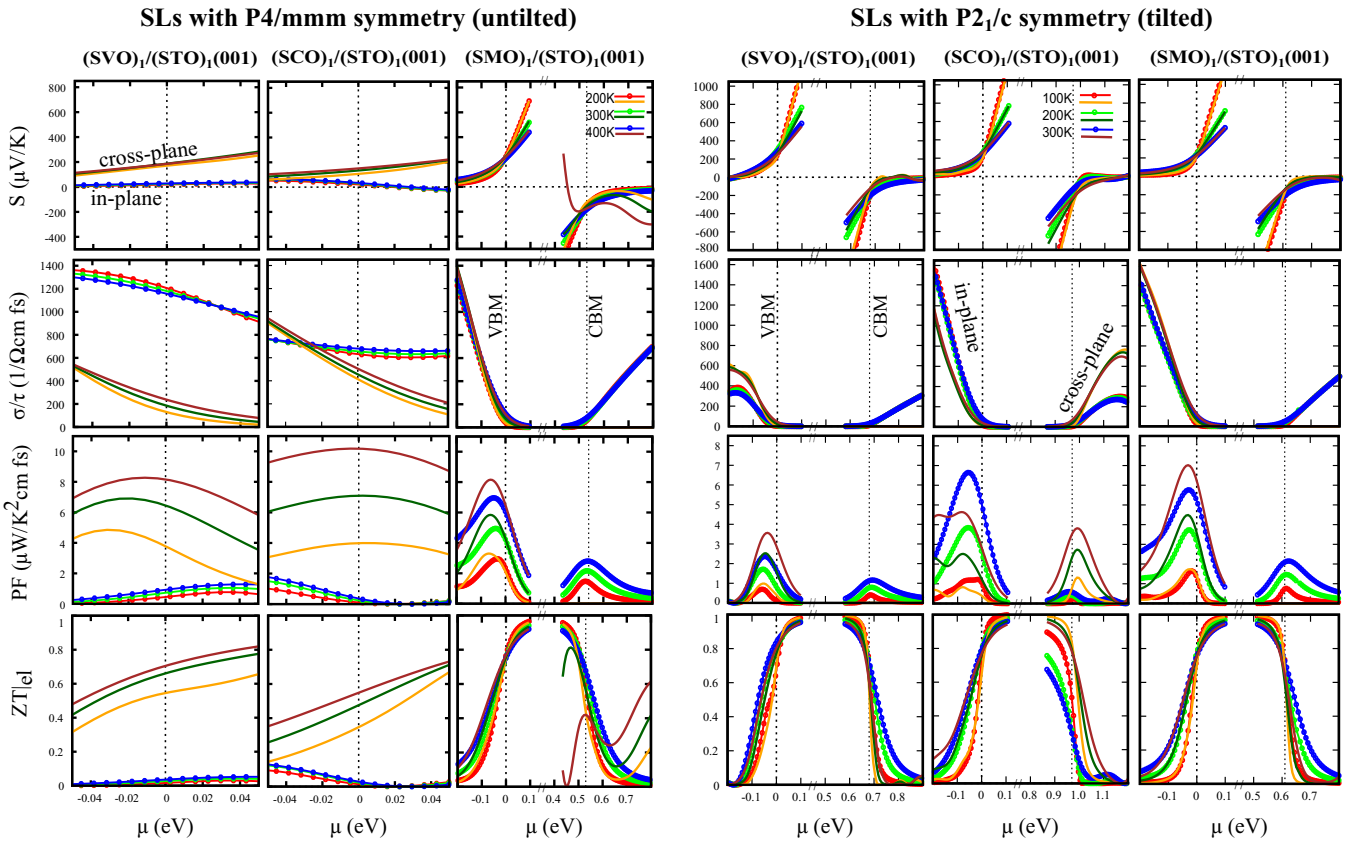

FIG. 6. Thermoelectric properties of $(SrXO_3)_1/(SrTiO_3)_1(001)$ SLs (X = V, Cr, and Mn) with $P4/mmm$ symmetry (absence of octahedral rotations, left panels) and $P2_1/c$ symmetry (including octahedral rotations, right panels). Three different temperatures are displayed in each case: 200, 300, and 400 K for the $P4/mmm$ SLs and 100, 200, and 300 K for the $P2_1/c$ SLs, reflecting the different temperature range where the SLs are expected to be stable. From top to bottom, Seebeck coefficient S, electrical conductivity σ/τ, power factor PF/τ, and electronic figure of merit $ZT|_{el}$ are shown, where τ denotes the relaxation time. Orange, dark-green, and brown lines (red, green, and blue lines with points) correspond to cross-plane (in-plane) transport. The vertical dashed line at zero energy denotes the Fermi level (if metallic) or the VBM (if semiconducting); in the latter case, the second vertical dashed line indicates the conduction band minimum (CBM).

find slightly enhanced PFs due to the (small) octahedral rotations at almost unchanged S, which is related to an increased electrical conductivity σ. For the $P2_1/c$ SLs, the Seebeck coefficients are in the range of 500–600 μV/K in all cases. Interestingly, we obtain similar in- and cross-plane values for S and PFs in the semiconducting systems near the VBM despite the layered crystal structure (Fig. 6). This resembles observations made in $(LNO)_1/(LAO)_1(001)$ SLs for S where, on the other hand, in- and cross-plane PFs were different due to the wide-gap LAO layer [22].

In general, we observe larger PFs for p-type than for n-type doping in the semiconducting systems since σ is found to be always higher near the VBM than near the CBM (Fig. 6). This is related to the O $2p$ states that constitute the valence band in the Mn-based SLs and the tilted Cr-based SLs and to the mentioned hybridization below E_F in the tilted V-based SL.

For the metallic systems, the electronic figure of merit $ZT|_{el} = \sigma S^2 T/\kappa_{el}$ attains cross-plane values of 0.8 and 0.7 for V and Cr, respectively. For the semiconducting systems, the usual convergence to $ZT|_{el} = 1$ is observed in the band gap. This is related to the electronic contribution to the thermal conductivity κ_{el}, which is found to follow the trend of the electrical conductivity σ. Although the calculation of the lattice thermal conductivity is beyond the scope of this paper, we note that the SL design is expected to favor phonon scattering in the vertical direction. This is supported by a recent experimental report of a large interface thermal resistance in $(SrVO_3)/(SrTiO_3)(001)$ SLs by Katsufuji *et al.* despite the similar phononic properties of the constituent bulk compounds [30].

We generally found an enhanced thermoelectric performance in the 1/1 SLs compared to the 1/3 SLs, particularly in the cross-plane direction due to the higher dispersion along Γ-Z. A detailed comparison demonstrating the influence of confinement (i.e., the STO thickness n) on the thermoelectric properties can be found in the Supplemental Material [68].

Finally, we compare the thermoelectric response of the 1/1 SLs around 300 K to some of the best-performing oxide thermoelectrics reported so far (Table II). The PFs obtained in this paper exceed the already large values reported for $(LNO)_1/(LAO)_1(001)$ SLs [22] by more than a factor of 2 and attain values that are comparable with those of La- and Nb-doped STO bulk and thin films [27–29]. Specifically, we point out 27.9 (26.6) μW K^{-2} cm^{-1} in plane for the Cr-based SL with $P4/mmm$ ($P2_1/c$) symmetry and 28.1 μW K^{-2} cm^{-1} cross plane for the Mn-based SL with $P2_1/c$ symmetry.

VII. SUMMARY

We combined density functional theory calculations including on-site Coulomb repulsion and Boltzmann transport theory in the constant relaxation time approximation to systematically explore the electronic, magnetic, and thermoelectric properties of $(SrXO_3)_1/(SrTiO_3)_n(001)$ superlattices, varying the number of confining spacer layers ($n = 1, 3$) and, particularly, the t_{2g} orbital occupation [X = V (d^1), Cr (d^2), and Mn (d^3)]. To disentangle the effect of quantum confinement and octahedral rotations and to account for a wider temperature range, we considered $P4/mmm$ (untilted) and $P2_1/c$ (tilted) phases and found that the ground-state superlattice geometries always display finite octahedral rotations. These drive a metal-to-insulator transition in confined $SrVO_3$ and $SrCrO_3$ single layers that is accompanied by an orbital reconstruction together with ferro- and antiferromagnetic spin alignments, respectively. On the other hand, a confined $SrMnO_3$ single layer shows electronic properties similar to bulk.

We demonstrated that the confinement favorably impacts the thermoelectric properties, particularly for $SrVO_3$ and $SrCrO_3$ due to the emergent Mott phase. Large room-temperature Seebeck coefficients were obtained for the tilted superlattices, ranging from 500 to 600 μV/K in the vicinity of the band edges. The estimated attainable power factors, for instance, 27.9 (26.6) $\mu W\,K^{-2}\,cm^{-1}$ in plane for the $(SrCrO_3)_1/(SrTiO_3)_1(001)$ superlattice with $P4/mmm$ ($P2_1/c$) symmetry and 28.1 $\mu W\,K^{-2}\,cm^{-1}$ cross plane for the $(SrMnO_3)_1/(SrTiO_3)_1(001)$ superlattice with $P2_1/c$ symmetry, compare favorably with some of the best-performing oxide thermoelectrics, such as La- or Nb-doped $SrTiO_3$. These findings prove that the enhancement of the thermoelectric response by exploiting confinement-induced metal-to-insulator transitions in short-period oxide superlattices [22] is a general principle that applies on a broader set of materials combinations.

ACKNOWLEDGMENTS

We acknowledge funding by the German Research Foundation (Deutsche Forschungsgemeinschaft, DFG) within the collaborative research center TRR 80 (Projektnummer 107745057), Projects No. G3 and No. G8. Computing time was granted by the Leibniz-Rechenzentrum, Garching bei München (Grant No. pr87ro).

[1] J. He, Y. Liu, and R. Funahashi, J. Mater. Res. **26**, 1762 (2011).
[2] S. Hébert and A. Maignan, in *Functional Oxides*, edited by D. W. Bruce, D. O'Hare, and (Wiley, Chichester, U.K., 2010).
[3] G. Pálsson and G. Kotliar, Phys. Rev. Lett. **80**, 4775 (1998).
[4] J. Merino and R. H. McKenzie, Phys. Rev. B **61**, 7996 (2000).
[5] P. Gorai, V. Stevanović, and E. S. Toberer, Nat. Rev. Mater. **2**, 17053 (2017).
[6] K. P. Ong, D. J. Singh, and P. Wu, Phys. Rev. Lett. **104**, 176601 (2010).
[7] R. F. Klie, Q. Qiao, T. Paulauskas, A. Gulec, A. Rebola, S. Öğüt, M. P. Prange, J. C. Idrobo, S. T. Pantelides, S. Kolesnik, B. Dabrowski, M. Ozdemir, C. Boyraz, D. Mazumdar, and A. Gupta, Phys. Rev. Lett. **108**, 196601 (2012).
[8] G. Xing, J. Sun, K. P. Ong, X. Fan, W. Zheng, and D. J. Singh, APL Mater. **4**, 053201 (2016).
[9] K. F. Garrity, Phys. Rev. B **94**, 045122 (2016).
[10] L. K. Lamontagne, G. Laurita, M. W. Gaultois, M. Knight, L. Ghadbeigi, T. D. Sparks, M. E. Gruner, R. Pentcheva, C. M. Brown, and R. Seshadri, Chem. Mater. **28**, 3367 (2016).
[11] M. E. Gruner, U. Eckern, and R. Pentcheva, Phys. Rev. B **92**, 235140 (2015).
[12] L. D. Hicks, T. C. Harman, and M. S. Dresselhaus, Appl. Phys. Lett. **63**, 3230 (1993).
[13] H. Y. Hwang, Y. Iwasa, M. Kawasaki, B. Keimer, N. Nagaosa, and Y. Tokura, Nature Mater. **11**, 103 (2012).
[14] J. Mannhart and D. G. Schlom, Science **327**, 1607 (2010).
[15] J. Chakhalian, A. J. Millis, and J. Rondinelli, Nature Mater. **11**, 92 (2012).
[16] S. Middey, J. Chakhalian, P. Mahadevan, J. Freeland, A. Millis, and D. Sarma, Annu. Rev. Mater. Res. **46**, 305 (2016).
[17] M. Lorenz *et al.*, J. Phys. D: Appl. Phys. **49**, 433001 (2016).
[18] I. Pallecchi, F. Telesio, D. Li, A. Fête, S. Gariglio, J.-M. Triscone, A. Filippetti, P. Delugas, V. Fiorentini, and D. Marré, Nat. Commun. **6**, 6678 (2015).
[19] D. I. Bilc, C. G. Floare, L. P. Zârbo, S. Garabagiu, S. Lemal, and P. Gosez, J. Phys. Chem. C **120**, 25678 (2016).
[20] A. Filippetti, P. Delugas, M. J. Verstraete, I. Pallecchi, A. Gadaleta, D. Marré, D. F. Li, S. Gariglio, and V. Fiorentini, Phys. Rev. B **86**, 195301 (2012).
[21] B. Geisler, A. Blanca-Romero, and R. Pentcheva, Phys. Rev. B **95**, 125301 (2017).
[22] B. Geisler and R. Pentcheva, Phys. Rev. Mater. **2**, 055403 (2018).
[23] B. Geisler and R. Pentcheva, Phys. Rev. Appl. **11**, 044047 (2019).
[24] A. Blanca-Romero and R. Pentcheva, Phys. Rev. B **84**, 195450 (2011).
[25] P. Delugas, A. Filippetti, M. J. Verstraete, I. Pallecchi, D. Marré, and V. Fiorentini, Phys. Rev. B **88**, 045310 (2013).
[26] H. Ohta, S. Kim, Y. Mune, T. Mizoguchi, K. Nomura, S. Ohta, T. Nomura, Y. Nakanishi, Y. Ikuhara, M. Hirano, H. Hosono, and K. Koumoto, Nature Mater. **6**, 129 (2007).
[27] B. Jalan and S. Stemmer, Appl. Phys. Lett. **97**, 042106 (2010).
[28] T. Okuda, K. Nakanishi, S. Miyasaka, and Y. Tokura, Phys. Rev. B **63**, 113104 (2001).
[29] S. Ohta, T. Nomura, H. Ohta, and K. Koumoto, J. Appl. Phys. **97**, 034106 (2005).
[30] T. Katsufuji, T. Saiki, S. Okubo, Y. Katayama, and K. Ueno, Phys. Rev. Mater. **2**, 051002(R) (2018).
[31] W. Kohn and L. J. Sham, Phys. Rev. **140**, A1133 (1965).
[32] P. Blaha, K. Schwarz, G. K. H. Madsen, D. Kvasnicka, and J. Luitz, WIEN2K, *an Augmented Plane Wave + Local Orbitals Program for Calculating Crystal Properties*, edited by K. Schwarz (Technische Universitat Wien, Vienna, 2001).
[33] J. P. Perdew, A. Ruzsinszky, G. I. Csonka, O. A. Vydrov, G. E. Scuseria, L. A. Constantin, X. Zhou, and K. Burke, Phys. Rev. Lett. **100**, 136406 (2008).

[34] V. I. Anisimov, I. V. Solovyev, M. A. Korotin, M. T. Czyzyk, and G. A. Sawatzky, Phys. Rev. B **48**, 16929 (1993).
[35] V. Pardo and W. E. Pickett, Phys. Rev. B **81**, 245117 (2010).
[36] K.-W. Lee and W. E. Pickett, Phys. Rev. B **80**, 125133 (2009).
[37] D. Doennig and R. Pentcheva, Sci. Rep. **5**, 7909 (2015).
[38] H. J. Monkhorst and J. D. Pack, Phys. Rev. B **13**, 5188 (1976).
[39] G. K. H. Madsen and D. J. Singh, Comput. Phys. Commun. **175**, 67 (2006).
[40] U. Sivan and Y. Imry, Phys. Rev. B **33**, 551 (1986).
[41] B. Geisler and P. Kratzer, Phys. Rev. B **92**, 144418 (2015).
[42] B. Geisler, P. Kratzer, and V. Popescu, Phys. Rev. B **89**, 184422 (2014).
[43] D. Comtesse, B. Geisler, P. Entel, P. Kratzer, and L. Szunyogh, Phys. Rev. B **89**, 094410 (2014).
[44] G. Shirane and Y. Yamada, Phys. Rev. **177**, 858 (1969).
[45] T. Maekawa, K. Kurosaki, and S. Yamanaka, J. Alloys Compd. **426**, 46 (2006).
[46] B. L. Chamberland and P. S. Danielson, J. Solid State Chem. **3**, 243 (1971).
[47] P. Dougier, J. C. C. Fan, and J. B. Goodenough, J. Solid State Chem. **14**, 247 (1975).
[48] M. Onoda, H. Ohta, and H. Nagasawa, Solid State Commun. **79**, 281 (1991).
[49] V. Giannakopoulou, P. Odier, J. M. Bassat, and J. P. Loup, Solid State Commun. **93**, 579 (1995).
[50] K. Yoshimatsu, T. Okabe, H. Kumigashira, S. Okamoto, S. Aizaki, A. Fujimori, and M. Oshima, Phys. Rev. Lett. **104**, 147601 (2010).
[51] Y. C. Lan, X. L. Che, and M. He, J. Alloys Compd. **354**, 95 (2003).
[52] I. H. Inoue, O. Goto, H. Makino, N. E. Hussey, and M. Ishikawa, Phys. Rev. B **58**, 4372 (1998).
[53] B. Chamberland, Solid State Commun. **5**, 663 (1967).
[54] A. C. Komarek, T. Möller, M. Isobe, Y. Drees, H. Ulbrich, M. Azuma, M. T. Fernández-Díaz, A. Senyshyn, M. Hoelzel, G. André, Y. Ueda, M. Grüninger, and M. Braden, Phys. Rev. B **84**, 125114 (2011).
[55] L. Ortega-San-Martin, A. J. Williams, J. Rodgers, J. P. Attfield, G. Heymann, and H. Huppertz, Phys. Rev. Lett. **99**, 255701 (2007).
[56] Z.-L. Zhu, J.-H. Gu, Y. Jia, and X. Hu, Physica B (Amsterdam) **407**, 1990 (2012).
[57] K. H. L. Zhang, Y. Du, P. V. Sushko, M. E. Bowden, V. Shutthanandan, L. Qiao, G. X. Cao, Z. Gai, S. Sallis, L. F. J. Piper, and S. A. Chambers, J. Phys.: Condens. Matter **27**, 245605 (2015).
[58] O. Chmaissem, B. Dabrowski, S. Kolesnik, J. Mais, D. E. Brown, R. Kruk, P. Prior, B. Pyles, and J. D. Jorgensen, Phys. Rev. B **64**, 134412 (2001).
[59] L. Suescun, O. Chmaissem, J. Mais, B. Dabrowski, and J. D. Jorgensen, J. Solid State Chem. **180**, 1698 (2007).
[60] T. Takeda and S. Ohara, J. Phys. Soc. Jpn. **37**, 275 (1974).
[61] R. Søndenå, P. Ravindran, S. Stølen, T. Grande, and M. Hanfland, Phys. Rev. B **74**, 144102 (2006).
[62] V. Caignaert, N. Nguyen, M. Hervieu, and B. Raveau, Mater. Res. Bull. **20**, 479 (1985).
[63] K. Kikuchi, H. Chiba, M. Kikuchi, and Y. Syono, J. Solid State Chem. **146**, 1 (1999).
[64] L. Maurel, N. Marcano, T. Prokscha, E. Langenberg, J. Blasco, R. Guzmán, A. Suter, C. Magén, L. Morellón, M. R. Ibarra, J. A. Pardo, and P. A. Algarabel, Phys. Rev. B **92**, 024419 (2015).
[65] P. Agrawal, J. Guo, P. Yu, C. Hébert, D. Passerone, R. Erni, and M. D. Rossell, Phys. Rev. B **94**, 104101 (2016).
[66] J. Bai, J. Yang, W. Dong, Y. Zhang, W. Bai, and X. Tang, Thin Solid Films **644**, 57 (2017).
[67] S. Smadici, P. Abbamonte, A. Bhattacharya, X. Zhai, B. Jiang, A. Rusydi, J. N. Eckstein, S. D. Bader, and J.-M. Zuo, Phys. Rev. Lett. **99**, 196404 (2007).
[68] See Supplemental Material at http://link.aps.org/supplemental/10.1103/PhysRevB.100.165126 for additional data on superlattices with $n = 3$ layers of $SrTiO_3$, the effect of spin-orbit coupling and charge disproportionation, the interplay of octahedral rotations, on-site Coulomb repulsion, and further structural data.
[69] I. I. Mazin, D. I. Khomskii, R. Lengsdorf, J. A. Alonso, W. G. Marshall, and R. M. Ibberson, A. Podlesnyak, M. J. Martínez-Lope, and M. M. Abd-Elmeguid, Phys. Rev. Lett. **98**, 176406 (2007).
[70] F. Wrobel, B. Geisler, Y. Wang, G. Christiani, G. Logvenov, M. Bluschke, E. Schierle, P. A. van Aken, B. Keimer, R. Pentcheva, and E. Benckiser, Phys. Rev. Mater. **2**, 035001 (2018).
[71] B. Geisler and P. Kratzer, Phys. Rev. B **88**, 115433 (2013).
[72] S. Matar, G. Demazeau, J. Sticht, V. Eyert, and J. Kübler, J. Phys. I (France) **2**, 315 (1992).
[73] S. Matar, V. Eyert, J. Sticht, J. Kübler, and G. Demazeau, J. Phys. I (France) **4**, 1199 (1994).
[74] M. De Raychaudhury, E. Pavarini, and O. K. Andersen, Phys. Rev. Lett. **99**, 126402 (2007).
[75] K. Maiti and D. D. Sarma, Phys. Rev. B **61**, 2525 (2000).
[76] T. Saitoh, A. E. Bocquet, T. Mizokawa, H. Namatame, A. Fujimori, M. Abbate, Y. Takeda, and M. Takano, Phys. Rev. B **51**, 13942 (1995).
[77] G. Zampieri, F. Prado, A. Caneiro, J. Briatico, M. T. Causa, M. Tovar, B. Alascio, M. Abbate, and E. Morikawa, Phys. Rev. B **58**, 3755 (1998).
[78] G. R. Blake, T. T. M. Palstra, Y. Ren, A. A. Nugroho, and A. A. Menovsky, Phys. Rev. B **65**, 174112 (2002).
[79] A. A. Tsvetkov, F. P. Mena, P. H. M. van Loosdrecht, D. van der Marel, Y. Ren, A. A. Nugroho, A. A. Menovsky, I. S. Elfimov, and G. A. Sawatzky, Phys. Rev. B **69**, 075110 (2004).
[80] M. Reehuis, C. Ulrich, P. Pattison, B. Ouladdiaf, M. C. Rheinstädter, M. Ohl, L. P. Regnault, M. Miyasaka, Y. Tokura, and B. Keimer, Phys. Rev. B **73**, 094440 (2006).
[81] G. Xing, J. Sun, Y. Li, X. Fan, W. Zheng, and D. J. Singh, Phys. Rev. Mater. **1**, 065405 (2017).